

Partially Oxidized Carbon Nanomaterials with Ni/NiO Heterostructures as Durable Glucose Sensors

Jinhang Xue, Cheng Han, Yuandong Yang, Shaojie Xu, Qipeng Li, Huagui Nie, Jinjie Qian,* and Zhi Yang*



Cite This: *Inorg. Chem.* 2023, 62, 3288–3296



Read Online

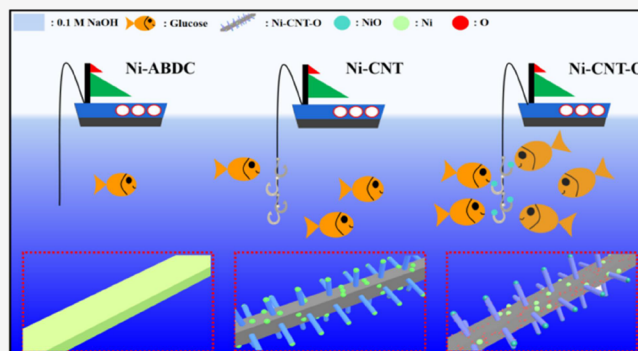
ACCESS |

Metrics & More

Article Recommendations

Supporting Information

ABSTRACT: Conventional enzyme-based glucose biosensors have limited extensive applications in daily life because glucose oxidase is easily inactivated and is expensive. In this paper, we propose a strategy to prepare a new type of cost-effective, efficient, and robust nonenzymatic Ni-CNT-O for electrochemical glucose sensing. It is first followed by the pyrolysis of Ni-ABDC nanostrips using melamine to grow carbon nanotubes (CNTs) to give an intermediate product of Ni-CNT, which is further accompanied by partial oxidation to enable the facile formation of hierarchical carbon nanomaterials with improved hydrophilicity. A series of physicochemical characterizations have fully proved that Ni-CNT-O is a carbon-coated heterostructure of Ni and NiO nanoparticles embedded into coordination polymer-derived porous carbons. The obtained Ni-CNT-O exhibits a better electrocatalytic activity for glucose oxidation stemming from the synergistic effect of a metal element and a metal oxide than unoxidized Ni-CNT, which also shows high performance with a wide linear range from 1 to 3000 μM . It also offers a high sensitivity of $79.4 \mu\text{A mM}^{-1} \text{cm}^{-2}$, a low detection limit of 500 nM ($S/N = 3$), and a satisfactory long-term durability. Finally, this glucose sensor exhibits good reproducibility, high selectivity, as well as satisfactory results by comparing the current response of simulated serum within egg albumen.



INTRODUCTION

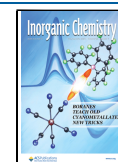
Previously, the International Diabetes Federation (IDF) released the latest version of "IDF World Diabetes Map (10th Edition)", mentioning that the total number of adults, 20–79 years old, living with diabetes reached more than 0.5 billion.¹ The prevention of diabetes and its complications becomes essential, particularly in middle-income countries, which is estimated to contribute to about 11.3% of deaths globally.^{2,3} In this context, long-term monitoring of blood glucose levels in susceptible populations is significantly required. Therefore, it is very necessary to develop a fast and accurate sensing platform to detect blood glucose levels in real time.^{4,5} Theoretically, the rapid detection of glucose can be performed by using enzymatic and nonenzymatic biosensors.^{6,7} Although enzyme-containing biosensors are intrinsically featured with high sensitivity and selectivity, glucose oxidase is not only expensive but also difficult to be activated stably, and the process of enzymatic loading is complicated, which hinders their application.^{8–10} Therefore, the rational design and exploitation of efficient nonenzymatic electrochemical biosensors based on nonprecious metal nanomaterials are highly anticipated.

Nonenzymatic electrochemical glucose-sensing materials with high accuracy, sensitivity, and efficiency have been

conveniently prepared based on relatively inexpensive and abundant transition metals (TMs).¹¹ Meanwhile, TM-based compounds, such as metal nitrides, oxides/hydroxides, phosphides, and so forth, have been demonstrated to provide rapid and sensitive responses toward glucose detection.^{11–14} On the other hand, it is well known that TM-based coordination polymers show a wider range of applications.^{15,16} They are often used as precursors and/or templates to fabricate metal–carbon nanomaterials with different structures and morphologies for energy storage as well as heterogeneous catalysis.^{17–19} However, with the continuous reaction using TM-based electrocatalysts for long-term chemical sensing, their overall nanostructures would be gradually destroyed and degraded, resulting in a slow disappearance of active species.²⁰ Therefore, nonenzymatic catalysts derived from TM-based coordination polymers need to be endowed with high activity as well as structural stability.

Received: December 20, 2022

Published: February 3, 2023



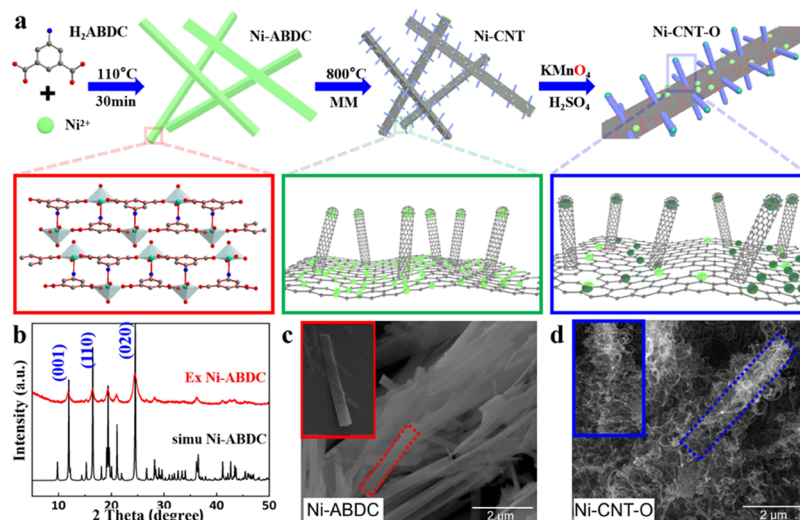


Figure 1. (a) Schematic diagram to obtain Ni-ABDC and its carbon derivatives; (b) PXRD patterns; SEM images of (c) Ni-ABDC and (d) Ni-CNT-O.

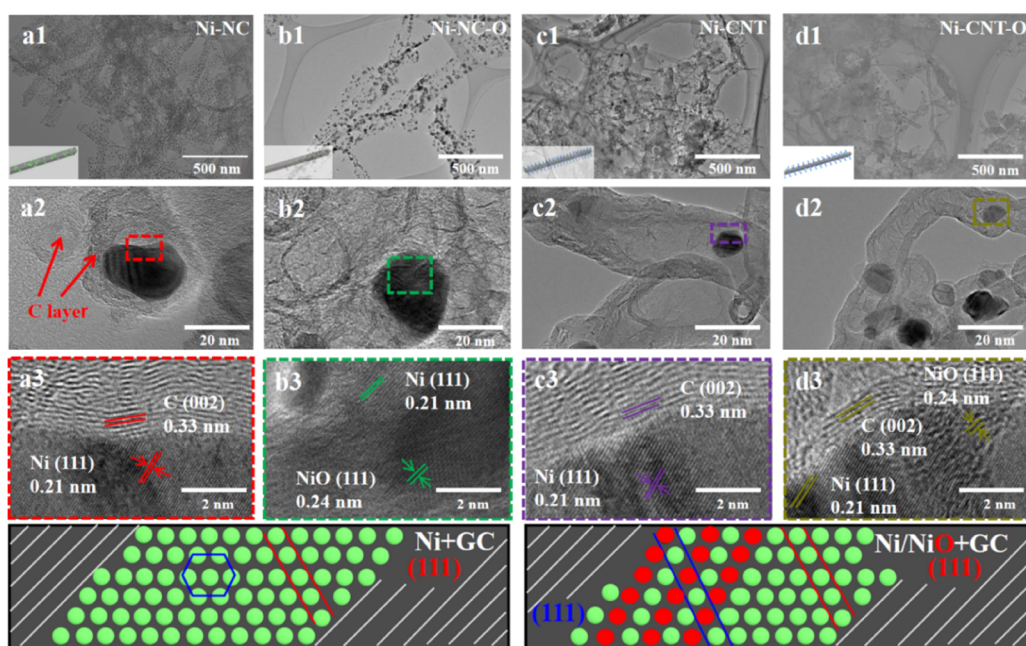


Figure 2. TEM and HR-TEM images of (a1–a3) Ni-NC, (b1–b3) Ni-NC-O, (c1–c3) Ni-CNT, and (d1–d3) Ni-CNT-O.

Carbon nanotubes (CNTs) are structurally featured with a hollow tubular nanostructure, large aspect ratio, significant electrical and mechanical properties, excellent stability, and good application prospects in glucose detection.^{21,22} However, pristine CNTs usually exhibit inferior performance in terms of glucose oxidation, as these in situ-formed metal nanoparticles (NPs) are fully protected inside the multilayer graphitic carbons.²³ From the point of view of growth mechanism, multifunctional CNTs are catalyzed by metals, which usually show a stable structure of carbon-coated metals that need to be activated before use for efficient glucose sensing.^{24,25} Furthermore, multiwalled CNTs are usually hydrophobic carbons, while glucose is hydrophilic, making CNTs poorly selective for the adsorption of glucose molecules.^{26,27} Under these circumstances, it remains a huge challenge to resolve the glucose affinity as well as the adequate exposure of active metal

species inside CNTs as nonenzymatic sensor materials to show a high activity, selectivity, as well as stability.

Here, a strip-like nickel-based coordination polymer, denoted as Ni-ABDC, can be conveniently synthesized by a solvothermal method. Through different thermal treatments, four types of porous carbon nanomaterials are obtained from the initial Ni-ABDC nanostrips, including Ni-NC, Ni-CNT, Ni-NC-O, and Ni-CNT-O. Among them, abundant CNTs are easily grown by the catalysis of in situ-formed nickel NPs that are anchored onto the carbon nanostrip of Ni-CNT. After being treated by acidic KMnO_4 , these carbon nanomaterials are further oxidized to give the final product Ni-CNT-O. In this case, the partially oxidized Ni-CNT-O not only exhibits high oxidative activity for glucose but also introduces oxygen-containing functional groups into rigid carbons, making it more hydrophilic and highly selective for electrocatalytic glucose detection.

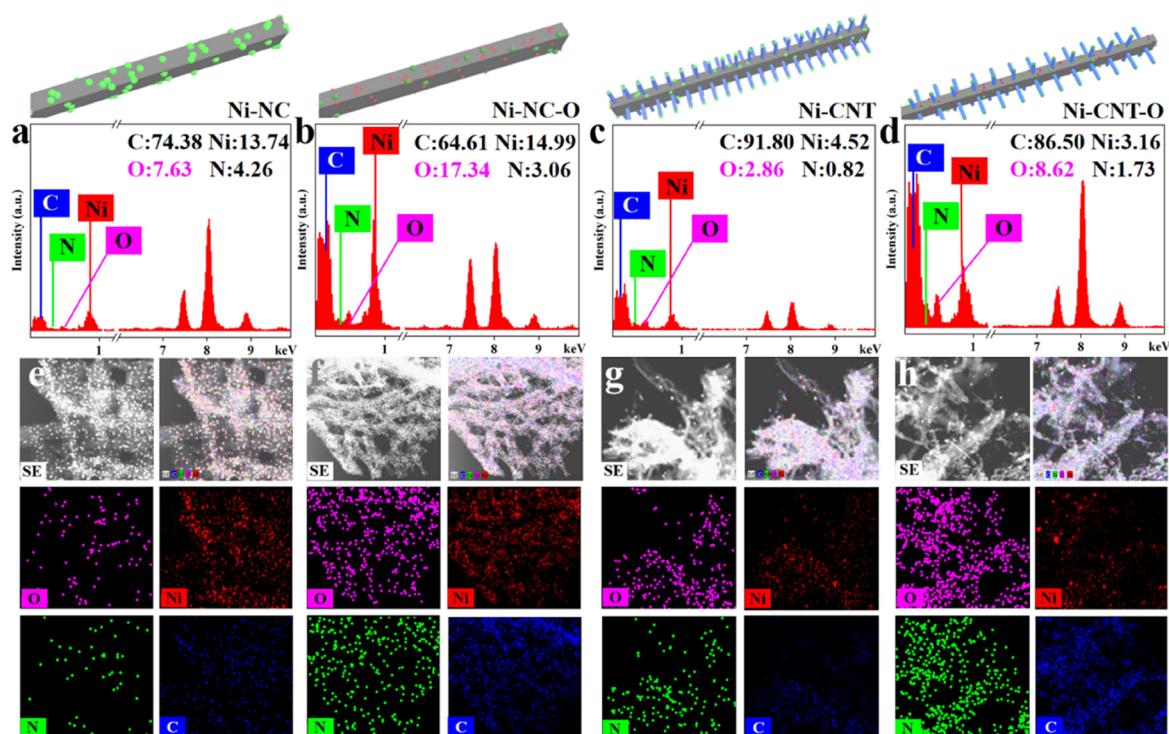


Figure 3. EDS spectra, HAADF-STEM images, and elemental mappings of (a, e) Ni-NC, (b, f) Ni-NC-O, (c, g) Ni-CNT and (d, h) Ni-CNT-O.

RESULTS AND DISCUSSION

First of all, nickel acetate and 5-aminomisophthalic acid (H_2ABDC) are used simultaneously to synthesize strip-like coordination polymers, as in Figure 1a and Table S1. For more details on the synthetic procedure of coordination polymers, refer to the Experimental part in the Supporting Information. The single-crystal structure of the Ni-ABDC precursor reveals that each ABDC^{2-} ligand uses its two carboxylates and one amino to bind to three adjacent Ni(II) ions that show the 6-coordinated octahedron geometry (Figure S2). In this 3D supermolecule, some moderate intermolecular interactions, including π - π stacking and hydrogen bonding, are clearly observed (Figure S3).²⁸ Three strong diffraction peaks at 12.1, 16.7, and 24.7°, namely (01 $\bar{1}$), (110), and (020) planes, indicate the successful growth of Ni-ABDC with highly crystalline properties, which presents a strip-shaped morphology along the *c*-axis, corresponding to the (01 $\bar{1}$) diffraction plane (Figures 1b,c, S4). In Figure S5, the obtained FT-IR spectrum is featured with two characteristic peaks, including the coordination bond (COO^- -Ni²⁺, 1610–1560 cm^{-1}) and N–H stretching (3237 cm^{-1}). On the other hand, porous Ni-NC and Ni-CNT are conveniently obtained by one-step pyrolysis. Further, the rapid growth of multiwalled CNTs could be achieved after adding melamine (MM) as the secondary carbon source as well as nitrogen source. During the thermal conversion, the original nanostrip can be well retained where abundant N-doped CNTs are grown onto Ni-NC through the efficient catalysis of in situ-formed Ni NPs. In Figure 1d, it is observed that the partial oxidation of carbon materials by KMnO_4 can not only introduce oxygen-containing functional groups but also remove extra inactive Ni species to give the final sample of Ni-CNT-O.^{29,30} In this case, the modification of CNTs would be beneficial to the better adsorption of guest molecules on the surface of catalysts that can dramatically improve subsequent performance.³¹

As shown in Figures S7 and S8, the SEM images show pristine Ni-ABDC nanostrips with an average width and length of 0.2 and 500 μm , respectively. Meanwhile, the carbonized Ni-NC and its partially oxidized Ni-NC-O maintain their initial shapes, but their surfaces become relatively rough after pyrolysis. Figures S9–S11 confirm the growth of numerous CNTs for Ni-CNT, and the TEM and HR-TEM images further reveal the nanostructure and morphological features of these carbon materials. In Figure 2a1–a3, Ni-NC is observed to exhibit a large number of Ni NPs anchored onto the carbon framework, but these particles that existed in Ni-NC-O are significantly less than those of the unoxidized counterpart, verifying the removal of inert Ni NPs by acid etching (Figure 2b1–b3). In addition, abundant N-doped CNTs are grown from melamine, while the growth of CNTs makes nickel particles encapsulated in graphitized carbons. Further, Ni-CNT-O does not show a massive loss of Ni NPs after being oxidized, and its morphology is also well preserved (Figure 2c1–c3, d1–d3). The HR-TEM images present two types of lattice fringe spacings of 0.33 and 0.21 nm assigned to the (002) plane of the graphitic carbon layer and the (111) plane of metallic Ni, respectively.^{32,33} In the meantime, Ni-NC-O and Ni-CNT-O which are partially oxidized by KMnO_4 give some visible fringes of 0.24 nm to the (111) plane of NiO. It should be noted that each sample shows the characteristic of the carbon layer to wrap the metal components, while the two oxidized samples are endowed with differentiated lattices between the graphitized carbons and Ni metals. Finally, AFM further reveals the calcined nanosheet shapes of 10–20 nm on average (Figure S12).

The EDXS spectra depict the coexistence of Ni, C, N, and O in Ni-NC, Ni-NC-O, Ni-CNT, and Ni-CNT-O (Figure 3a–d). For partial oxidation, both the oxygen concentrations of Ni-NC-O (17.34 at%) and Ni-CNT-O (8.62 at%) are much higher than those of the corresponding unoxidized samples

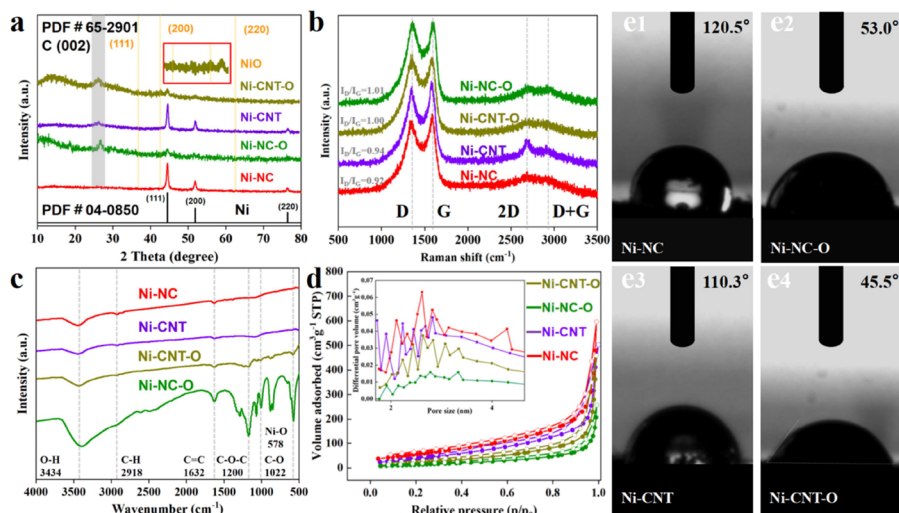


Figure 4. (a) PXRD patterns; (b) Raman spectra; (c) FT-IR curves; (d) N_2 isotherms and their corresponding PSD; and (e1–e4) contact angle measurements for Ni-NC, Ni-NC-O, Ni-CNT, and Ni-CNT-O.

(Ni-NC, 7.63 at%; Ni-CNT, 2.86 at%). However, the nickel contents of Ni-CNT (4.52 at%) and Ni-CNT-O (3.16 at%) become significantly lower compared to the control samples as a result of efficient CNT growth. On the other hand, the collected elemental mapping images in Figure 3e–h verify the uniform distribution of these four elements. It is obvious that after the rapid growth of CNTs, the content of carbon increases significantly, and the content of O element can also be correspondingly increased by simple oxidation with potassium permanganate.³⁴ The above observations are indicative of the successful formation of hierarchically porous carbon nanostrips with highly conductive CNTs and rich nickel species in Ni-CNT-O. Therefore, it would be conducive to the rapid transportation of electrons as well as exposure of active sites that facilitate efficient electrochemical reactions.

The structural phases and components of these nanocomposites are further determined using PXRD analysis. Both unoxidized Ni-NC and Ni-CNT have sharp diffraction peaks at 44.5° , originating from the (111) plane of metallic Ni (PDF#04-0850). Although the diffraction patterns of Ni-NC-O and Ni-CNT-O retain the characteristic peaks of nickel metal after oxidation, they show an obvious destruction of crystallinity (Figure 4a). The diffraction intensity decreases, and two emerging but weak signals at 36.9 and 42.9° are attributed to the (111) and (200) planes of NiO (PDF#65-2901), respectively. In Figure 4b, Raman spectra exhibit two representative bands at 1350 and 1587 cm^{-1} , ascribed to the disordered sp^3 -carbon (D-band) and graphitic sp^2 -carbon (G-band). It is noted that the graphitization degree (I_D/I_G) becomes less after oxidation to imply the introduction of oxygen atoms (Ni-NC, 0.92; Ni-NC-O, 1.01; Ni-CNT, 0.94; and Ni-CNT-O, 1.00). FT-IR analysis also reveals that these oxidized samples own sharp peaks corresponding to the C–O and C–O–C bonds at 1022 and 1200 cm^{-1} in Figure 4c, respectively. Furthermore, based on the N_2 sorption isotherms and pore size distribution (PSD), the pore size of Ni-CNT-O is observed to be more concentrated at 2–4 nm compared to the pristine CNTs (Figure 4d and Table S2).

Finally, both the partially oxidized Ni-NC-O and Ni-CNT-O are relatively hydrophilic with smaller contact angles of 53.0 and 45.5° in comparison to Ni-NC (120.5°) and Ni-CNT (110.3°), respectively. Although the adsorption capacity of the

material decreases slightly due to the increase of oxygen atoms, the formation of more mesopores as well as less hydrophobic properties for Ni-CNT-O would speed up the entry of electrolytes as well as guest molecules for efficient sensor performance (Figure S13).

To reveal the constituent elements and coordination environment of this series of carbon nanomaterials, X-ray photoelectron spectroscopy (XPS) is further performed. First of all, the full survey spectra verify the presence of Ni, C, N, and O elements, where the O 1s signal increases significantly after the partial oxidation. In the meantime, owing to the protective effect of multiwalled CNTs, the oxygen content of Ni-CNT-O tends to be slightly lower than that of Ni-NC-O (Figure 5a).^{35,36} For Ni-CNT-O, the high-resolution Ni 2p curve clearly shows the dominant presence of metallic Ni(0) at 852.8 and 868.8 eV, while two small peaks at 854.3 and 872.1 eV are reasonably assigned to Ni(II) $2p_{3/2}$ and $2p_{1/2}$, respectively (Figure 5b). The deconvoluted O 1s curves of Ni-CNT-O and Ni-NC-O have larger areas than those of Ni-CNT and Ni-NC on account of the successful occurrence of oxidation. It shows three broad peaks at 529.5, 531.2, and 533 eV that are attributed to Ni–O, C=O/C–O–C, and C–O bonds, respectively. In this case, the generation of NiO species onto the surface of Ni NPs gives rich NiO/Ni heterostructures that would accelerate electron transport (Figure 5c).³⁷ Besides, one broad peak of C 1s spectrum can be divided into 284.8, 285.5, 288.8, and 291.2 eV, belonging to the C–C/C=C, C–O, O–C=O, and π – π^* shake-up in Figure 5d, respectively. In Figure 5e, the N 1s can also be separated into four peaks at 398.0, 399.2, 401.0, and 402.1 eV, which are ascribed to pyridinic N, pyrrolic N, graphitic N, and oxidized N, respectively.

To study the electrocatalytic glucose oxidation, Ni-CNT-O is first dispersed in H_2O /Nafion/EtOH solution and immobilized onto a glassy carbon electrode. The results show that the anodic and cathodic peaks increase within 5 – 50 mV s^{-1} that presents a good linear relationship between the peak current and the square root of the scan rate (Figure 6a). In Figure 6b, the cyclic voltammetry (CV) curves with different glucose concentrations are collected from 0.0 to 0.8 V vs Ag/AgCl. The corresponding calibration curve for the anodic peak current is linearly correlated with the glucose

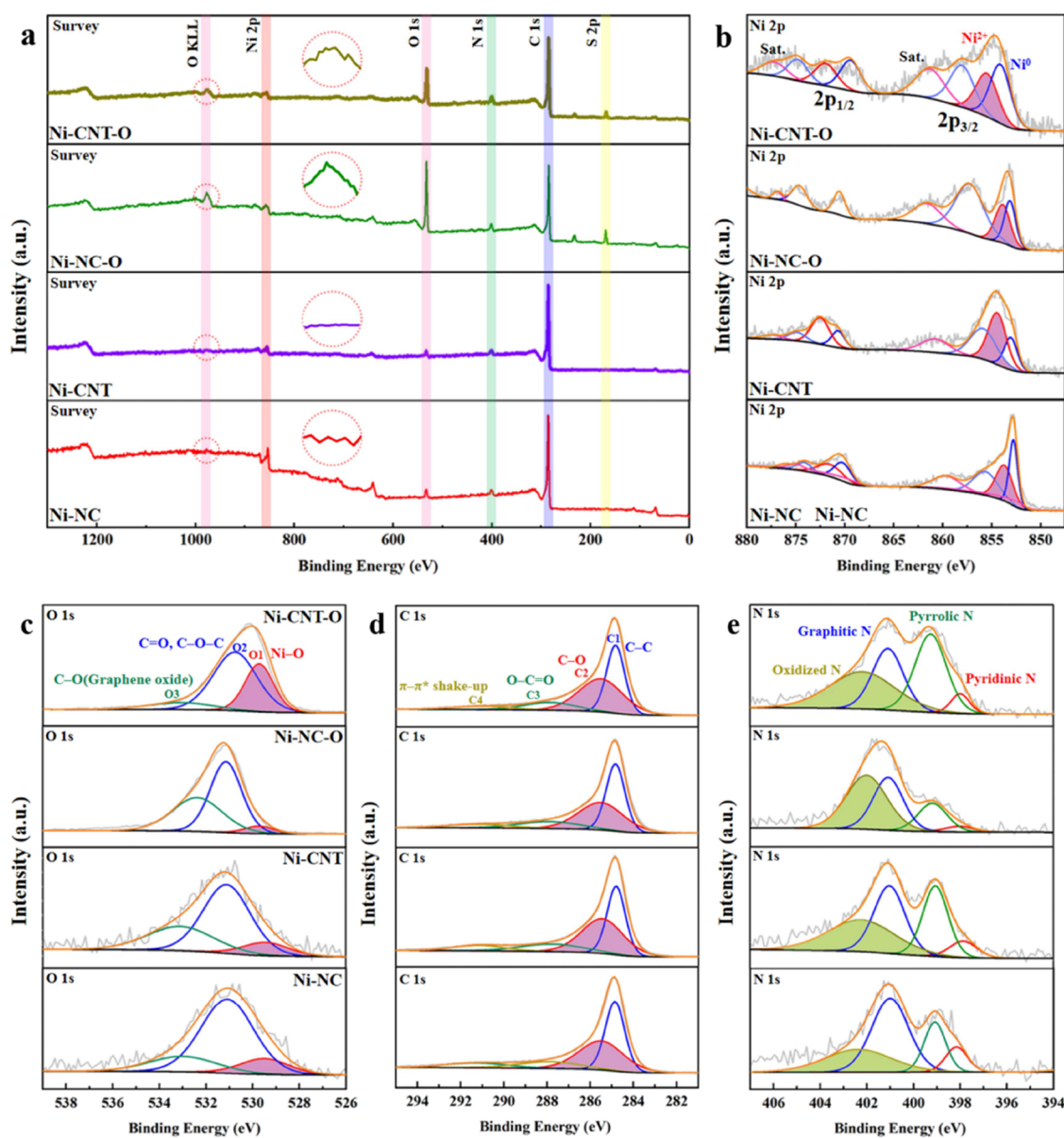


Figure 5. (a) Full survey XPS spectra and the deconvoluted spectra of (b) Ni 2p, (c) O 1s, (d) C 1s, and (e) N 1s.

concentration range ($A_2 = 0.997$ and $C_2 = 0.999$) from 1.0 to 5.0 mM (Figure 6b inset), confirming the excellent electrocatalytic performance. The enhancement of anodic current partially stems from the electro-oxidation of glucose with the participation of Ni(III) centers as follows: $\text{Ni(II)-CNT-O} \rightarrow \text{Ni(III)-CNT-O} + e$; $\text{Ni(III)-CNT-O} + \text{OH}^- + \text{glucose} \rightarrow \text{Ni(II)-CNT-O} + \text{gluconolactone} + \text{H}_2\text{O} + e$.³⁸ In Figure 6c, Ni-CNT-O exhibits the largest redox peak potential difference under the same loading at 10 mV s^{-1} to reflect its high electrochemical activity of the electrode surface. In order to verify its applicability, the electrocatalytic activity of Ni-CNT-O-modified electrodes on glucose is investigated in Figure S14. Amperometric measurements by continuously adding $100 \mu\text{M}$ glucose give a steady-state and maximum current intensity at 0.58 V (Figure S15). Meanwhile, Figure 6d shows the current response to continuous injection of different concentrations of glucose in 0.1 M NaOH at 0.58 V . A clear, fast, and stable current response can be observed by continuously instilling glucose for Ni-CNT-O, showing a better electrochemical

response compared to that of other three control samples where the oxidation current and glucose concentration present a linear relationship (Figure 6e,g). Ni-CNT-O exhibits a more positive linear response range between $1 \mu\text{M}$ and 3 mM as $I = 26.18C + 4.45$, where C (μM) and I (mA) are the glucose concentration and current density, respectively. Figures 6f and S16 depict a significant current response to glucose (1 mM) but a small and almost negligible current response to the interferents (0.1 mM), including uric acid (UA), D-fructose, and sucrose.^{39,40} The calibration curve shows a linear range of $1 \mu\text{M}$ to 3 mM and a low detection limit of 500 nM at the signal-to-noise ratio of 3. A sensitivity of $79.4 \mu\text{A mM}^{-1} \text{ cm}^{-2}$ is obtained by dividing the slope of the linear regression equation by the electroactive surface area (Figures 6g, S17, and S18).⁴¹ The electrochemical impedance spectroscopy analysis shows that Ni-CNT-O has a smaller resistance than the other control samples (Figure S19). Furthermore, glucose and egg albumen are further mixed to evaluate the feasibility of Ni-CNT-O for human serum (Figure 6h,i and Table 1). In this

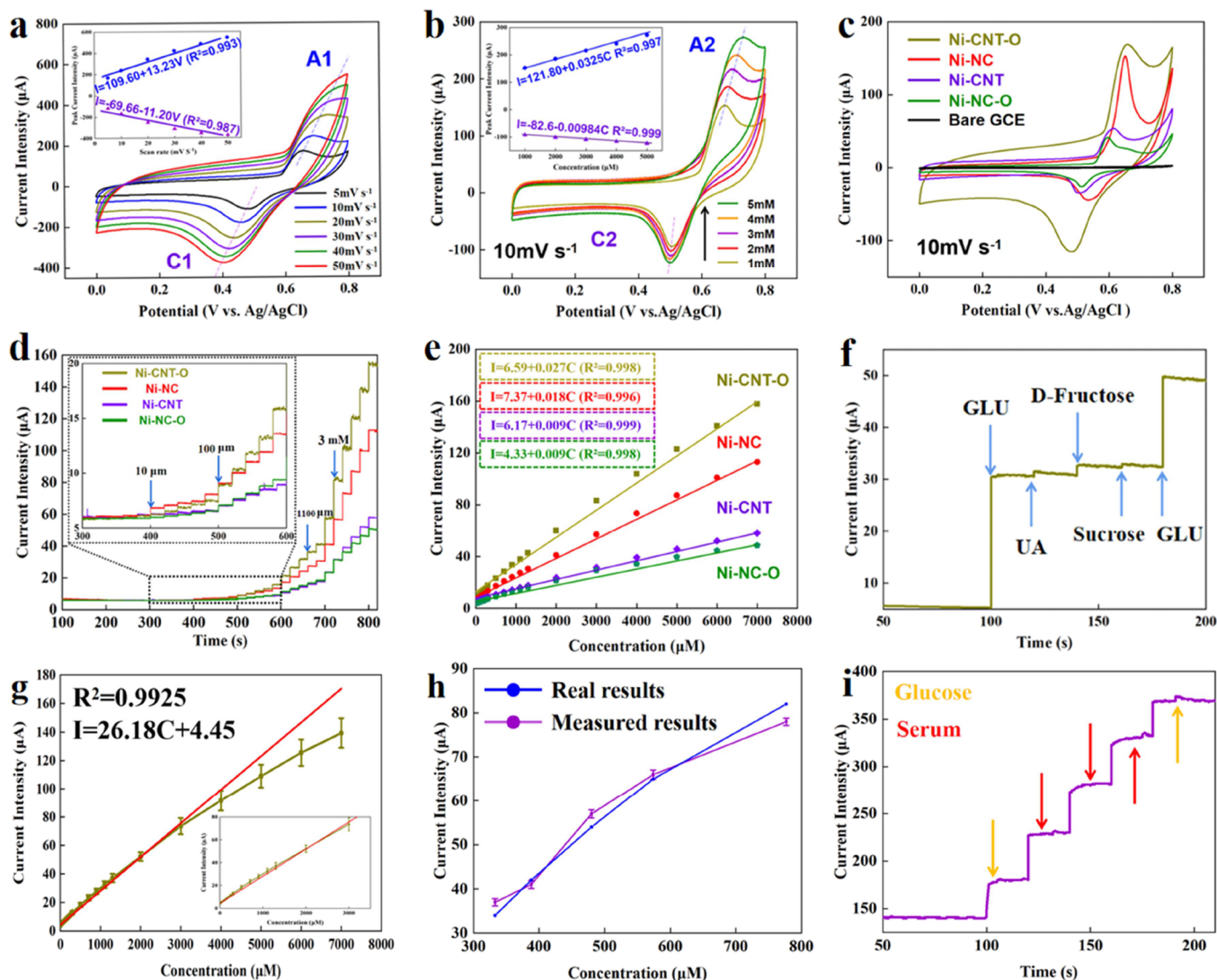


Figure 6. CV curves (a) with different scanning rates, (b) after inserting different concentrations for Ni-CNT-O. (c) All involved test materials. The current responses (d) with successive addition of glucose, (e) in 0.01–7 mM, (f) with different interferences. (g) Corresponding linear curve of Ni-CNT-O/GCE for the detection of glucose at 0.58 V. (h, i) Glucose detection comparison and response curves of samples.

Table 1. Comparison of Glucose Values in Real Serum Samples with Those Detected Ones by Our Glucose Sensor

sample	content of each component		
1	GLU (388 $\mu\text{mol L}^{-1}$) + serum (50 μL) + NaOH (5 mL)		
2	GLU (574 $\mu\text{mol L}^{-1}$) + serum (50 μL) + NaOH (5 mL)		
3	GLU (480 $\mu\text{mol L}^{-1}$) + serum (50 μL) + NaOH (5 mL)		
4	GLU (333 $\mu\text{mol L}^{-1}$) + serum (50 μL) + NaOH (5 mL)		
5	GLU (777 $\mu\text{mol L}^{-1}$) + serum (50 μL) + NaOH (5 mL)		
sample	measured results (mA) ^a	compared results (mA) ^b	relative error (%) ^c
1	0.042	0.041	-2.3%
2	0.062	0.066	6.0%
3	0.054	0.057	5.2%
4	0.034	0.037	8.1%
5	0.082	0.078	-5.1%

^aTested by the obtained Ni-CNT-O-based sensor. ^bCalculated by the real serum. ^cThe difference between the measured and compared results divided by the compared results.

case, the current responses of these five samples are determined to be 0.042, 0.062, 0.054, 0.034, and 0.082 mM,

which are very close to the actual glucose concentrations (0.041, 0.066, 0.057, 0.037, and 0.078 mM), with a satisfactory glucose detection ability from 1 to 50 days (Figure S20). It is indicated that the prepared sensor can be potentially used for routine glucose analysis in real biological samples with good accuracy and precision, which is competitive to the sensors reported in Table S3. The reported glucose sensors are often difficult to accommodate adequate linear ranges due to high response, which will severely limit their practical applications. In this work, the obtained Ni-CNT-O exhibits sufficient response as well as a wide linear range, which shows great prospects in the practical use of the sensor scenarios.

Finally, theoretical calculations have also further investigated the role of Ni/NiO heterostructures in promoting glucose oxidation by constructing two carbon models of Ni-CNT and Ni-CNT-O in Figure 7a,b. According to the following equation, $E_a = E_{\text{CNT-Ni/NiO-glucose}} - E_{\text{CNT-Ni/NiO}} - E_{\text{glucose}}$, the adsorption energies (E_a) of glucose molecules on the surface are calculated to be -2.022 and -3.182 eV for Ni-CNT and Ni-CNT-O, respectively. More details on the computational calculations are provided in the Supporting Information. In this

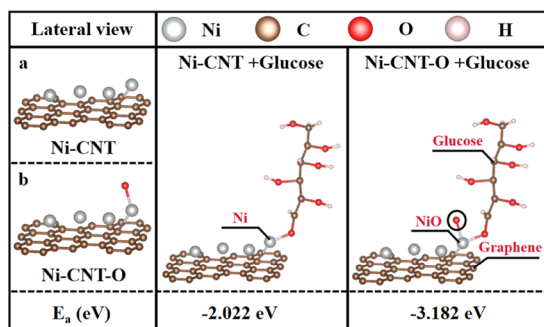


Figure 7. Theoretical calculation studies of (a) optimized nanostructures of Ni-CNT and Ni-CNT-O; (b) optimized glucose adsorption sites.

case, negative E_a values imply that the adsorption of glucose on the catalyst surface is energetically favorable.

On the other hand, the E_a value of Ni-CNT-O is smaller than that of Ni-CNT, indicating that the in situ formation of the Ni/NiO heterostructure is more favorable for glucose adsorption than pure Ni catalysts, which would lead to the improvement of glucose detection.

CONCLUSIONS

In summary, we have synthesized porous Ni-CNT by the pyrolysis of a strip-shaped Ni-ABDC coordination polymer that endows an efficient growth of CNTs using melamine at a high temperature. Through the partial oxidation of KMnO_4 , the obtained Ni-CNT-O can not only introduce oxygen-containing functional groups but also remove extra inactive Ni species to achieve efficient glucose detection. The optimal electrocatalyst of Ni-CNT-O is a highly sensitive glucose sensor ($79.4 \mu\text{A mM}^{-1} \text{cm}^{-2}$) with a wide detection range (1 μM to 3 mM), low detection limit (500 nM), and good long-term durability (>50 days) compared with the control samples. In addition, satisfactory results are obtained by comparing the response of the simulated serum with that of the real glucose content. In this work, the effective combination of Ni/NiO heterostructures and conductive CNTs with oxygen-containing species greatly improves the electrochemical performance, making Ni-CNT-O a strong competitor for practical application in biosensors. This work shows the unique advantages and broad potential of modifying coordination polymer-derived carbon nanomaterials by partial oxidation for efficient nonenzymatic glucose detection.

ASSOCIATED CONTENT

Supporting Information

The Supporting Information is available free of charge at <https://pubs.acs.org/doi/10.1021/acs.inorgchem.2c04445>.

Experimental and computational details, coordination environment and crystal data, and TGA, SEM/TEM, AFM, FT-IR, and electrochemical data (PDF)

AUTHOR INFORMATION

Corresponding Authors

Jinjie Qian – College of Life and Environmental Science, Wenzhou University, Wenzhou 325000, P. R. China; orcid.org/0000-0002-9996-7929; Email: jinjieqian@wzu.edu.cn

Zhi Yang – College of Life and Environmental Science, Wenzhou University, Wenzhou 325000, P. R. China; Email: yangzhi@wzu.edu.cn

Authors

Jinhang Xue – College of Life and Environmental Science, Wenzhou University, Wenzhou 325000, P. R. China; Key Laboratory of Carbon Materials of Zhejiang Province, College of Chemistry and Materials Engineering, Wenzhou University, Wenzhou, Zhejiang 325000, P. R. China

Cheng Han – College of Life and Environmental Science, Wenzhou University, Wenzhou 325000, P. R. China

Yuandong Yang – College of Life and Environmental Science, Wenzhou University, Wenzhou 325000, P. R. China; Key Laboratory of Carbon Materials of Zhejiang Province, College of Chemistry and Materials Engineering, Wenzhou University, Wenzhou, Zhejiang 325000, P. R. China

Shaojie Xu – College of Life and Environmental Science, Wenzhou University, Wenzhou 325000, P. R. China

Qipeng Li – Science and Technology Department, College of Chemistry and Chemical Engineering, Zhaotong University, Zhaotong, Yunnan 657000, P. R. China; orcid.org/0000-0002-8792-0592

Huagui Nie – College of Life and Environmental Science, Wenzhou University, Wenzhou 325000, P. R. China

Complete contact information is available at:

<https://pubs.acs.org/10.1021/acs.inorgchem.2c04445>

Author Contributions

All authors contributed extensively to this work. J.Q. and Z.Y. conceived the research project. J.X. conducted the experiments and performed the characterization studies. J.X. wrote the manuscript, with input from the other authors. All authors have given approval to the final version of the manuscript.

Notes

The authors declare no competing financial interest.

ACKNOWLEDGMENTS

This work was financially supported by National Natural Science Foundation of China (21601137), Natural Science Foundation of Zhejiang Province (LQ16B010003), Basic Science and Technology Research Project of Wenzhou, Zhejiang Province (G20190007), and the Special Basic Cooperative Research Programs of Yunnan Provincial Undergraduate Universities Association (202101BA070001-042).

REFERENCES

- Ogle, G. D.; James, S.; Dabelea, D.; Pihoker, C.; Svensson, J.; Maniam, J.; Klatman, E. L.; Patterson, C. C. Global estimates of incidence of type 1 diabetes in children and adolescents: Results from the International Diabetes Federation Atlas, 10th edition. *Diabetes Res. Clin. Pract.* **2022**, *183*, 109083–109092.
- Pillay, J.; Donovan, L.; Guitard, S.; Zakher, B.; Gates, M.; Gates, A.; Vandermeer, B.; Bougatsos, C.; Chou, R.; Hartling, L. Screening for Gestational Diabetes. *JAMA* **2021**, *326*, 539–562.
- Cole, J. B.; Florez, J. C. Genetics of diabetes mellitus and diabetes complications. *Nat. Rev. Nephrol.* **2020**, *16*, 377–390.
- Sabu, C.; Henna, T. K.; Raphey, V. R.; Nivitha, K. P.; Pramod, K. Advanced biosensors for glucose and insulin. *Biosens. Bioelectron.* **2019**, *141*, 111201–111222.
- Bag, S.; Bakshi, A.; Nandam, S. H.; Wang, D.; Ye, X. L.; Ghosh, J.; Pradeep, T.; Hahn, H. Nonenzymatic Glucose Sensing Using $\text{Ni}_{60}\text{Nb}_{40}$ Nanoglass. *ACS Nano* **2020**, *14*, 5543–5552.

- (6) Lee, W. C.; Kim, K. B.; Gurudatt, N. G.; Hussain, K. K.; Choi, C. S.; Park, D. S.; Shim, Y. B. Comparison of enzymatic and non-enzymatic glucose sensors based on hierarchical Au-Ni alloy with conductive polymer. *Biosens. Bioelectron.* **2019**, *130*, 48–54.
- (7) Teymourian, H.; Barfidokht, A.; Wang, J. Electrochemical glucose sensors in diabetes management: an updated review (2010–2020). *Chem. Soc. Rev.* **2020**, *49*, 7671–7709.
- (8) Feng, T.; Yu, C. F.; Kabtamu, D. M.; Bu, L.; Li, F. T.; Wang, Y. Cu₂O nanowires with exposed {111} facet for nonenzymatic detection of glucose in complex biological fluids. *Chem. Eng. J.* **2022**, *429*, 132267–132277.
- (9) Zhou, Y.; Hu, Q.; Yu, F.; Ran, G. Y.; Wang, H. Y.; Shepherd, N. D.; D'Alessandro, D. M.; Kurmoo, M.; Zuo, J. L. A Metal–Organic Framework Based on a Nickel Bis(dithiolene) Connector: Synthesis, Crystal Structure, and Application as an Electrochemical Glucose Sensor. *J. Am. Chem. Soc.* **2020**, *142*, 20313–20317.
- (10) Shen, L.; Liang, Z.; Chen, Z. Y.; Wu, C.; Hu, X. F.; Zhang, J. Y.; Jiang, Q.; Wang, Y. B. Reusable electrochemical non-enzymatic glucose sensors based on Au-inlaid nanocages. *Nano Res.* **2022**, *15*, 6490–6499.
- (11) Myndrul, V.; Coy, E.; Babayevska, N.; Zahorodna, V.; Balitskiy, V.; Baginskiy, I.; Gogotsi, O.; Bechelany, M.; Giardi, M. T.; Iatsunskiy, I. MXene nanoflakes decorating ZnO tetrapods for enhanced performance of skin-attachable stretchable enzymatic electrochemical glucose sensor. *Biosens. Bioelectron.* **2022**, *207*, 114141–114153.
- (12) Xue, J. H.; Sun, Q. H.; Li, Q. P.; Qian, J. J. MOF-derived carbon-coated cuprous phosphide nanosheets for electrocatalytic glucose oxidation. *CrystEngComm* **2022**, *24*, 3649–3655.
- (13) Gayathri, S.; Arunkumar, P.; Kim, J.; Han, J. H. Bimetallic Layered Hydroxide Nitrate@Graphene Oxide as an Electrocatalyst for Efficient Non-Enzymatic Glucose Sensors: Tuning Sensitivity by Hydroxide-Regulated M₂(OH)_{4–n}(Aⁿ⁻) Phases Derived from Solvent Engineering. *ACS Sustainable Chem. Eng.* **2022**, *10*, 1689–1701.
- (14) Yang, P.; Wang, X.; Ge, C. Y.; Fu, X.; Liu, X. Y.; Chai, H. X.; Guo, X. L.; Yao, H. C.; Zhang, Y. X.; Chen, K. Fabrication of CuO nanosheets-built microtubes via Kirkendall effect for non-enzymatic glucose sensor. *Appl. Surf. Sci.* **2019**, *494*, 484–491.
- (15) Zhou, Y.; Liu, H.; Gu, X. C.; Wu, X.; Feng, L. G. Hetero MOF-on-MOF-derived carbon nanotube interconnected nitrogen-doped carbon-encapsulated FeNi/FeF₂ for efficient oxygen evolution reaction. *Carbon Energy* **2022**, *4*, 924–938.
- (16) Kirchon, A.; Feng, L.; Drake, H. F.; Joseph, E. A.; Zhou, H. C. From fundamentals to applications: a toolbox for robust and multifunctional MOF materials. *Chem. Soc. Rev.* **2018**, *47*, 8611–8638.
- (17) Wang, X.; Dong, A.; Hu, Y.; Qian, J.; Huang, S. A review of recent work on using metal-organic frameworks to grow carbon nanotubes. *Chem. Commun.* **2020**, *56*, 10809–10823.
- (18) Chen, T. T.; Wang, F. F.; Cao, S.; Bai, Y.; Zheng, S. S.; Li, W. T.; Zhang, S. T.; Hu, S. X.; Pang, H. In Situ Synthesis of MOF-74 Family for High Areal Energy Density of Aqueous Nickel-Zinc Batteries. *Adv. Mater.* **2022**, *34*, No. 2201779.
- (19) Chai, L.; Hu, Z.; Wang, X.; Zhang, L.; Li, T.-T.; Hu, Y.; Pan, J.; Qian, J.; Huang, S. Fe₃C₃ nanoparticles with in situ grown CNT on nitrogen doped hollow carbon cube with greatly enhanced conductivity and ORR performance for alkaline fuel cell. *Carbon* **2021**, *174*, 531–539.
- (20) Shen, K.; Chen, X. D.; Chen, J. Y.; Li, Y. W. Development of MOF-Derived Carbon-Based Nanomaterials for Efficient Catalysis. *ACS Catal.* **2016**, *6*, 5887–5903.
- (21) Zhu, T. X.; Zhang, Y. F.; Luo, L. Q.; Zhao, X. L. Facile Fabrication of NiO-Decorated Double-Layer Single-Walled Carbon Nanotube Buckypaper for Glucose Detection. *ACS Appl. Mater. Interfaces* **2019**, *11*, 10856–10861.
- (22) Cella, L. N.; Chen, W.; Myung, N. V.; Mulchandani, A. Single-Walled Carbon Nanotube-Based Chemiresistive Affinity Biosensors for Small Molecules: Ultrasensitive Glucose Detection. *J. Am. Chem. Soc.* **2010**, *132*, 5024–5026.
- (23) Zhang, F.; Hou, P. X.; Liu, C.; Wang, B. W.; Jiang, H.; Chen, M. L.; Sun, D. M.; Li, J. C.; Cong, H. T.; Kauppinen, E. I.; Cheng, H. M. Growth of semiconducting single-wall carbon nanotubes with a narrow band-gap distribution. *Nat. Commun.* **2016**, *7*, 11160.
- (24) Gupta, P.; Gupta, V. K.; Huseinov, A.; Rahm, C. E.; Gazica, K.; Alvarez, N. T. Highly sensitive non-enzymatic glucose sensor based on carbon nanotube microelectrode set. *Sens. Actuators B: Chem.* **2021**, *348*, No. 130688.
- (25) Schroeder, V.; Savagatrup, S.; He, M.; Lin, S.; Swager, T. M. Carbon Nanotube Chemical Sensors. *Chem. Rev.* **2019**, *119*, 599–663.
- (26) Fan, H. L.; Wang, J. X.; Wu, P. P.; Zheng, L.; Xiang, J. F.; Liu, H. L.; Han, B. X.; Jiang, L. Superamphiphilicity for reducing diffusion resistance in liquid-liquid catalysis systems. *Chem* **2021**, *7*, 1852–1869.
- (27) Hummer, G.; Rasaiah, J. C.; Noworyta, J. P. Water conduction through the hydrophobic channel of a carbon nanotube. *Nature* **2001**, *414*, 188–190.
- (28) Chen, D. D.; Han, C.; Sun, Q. H.; Ding, J. Y.; Huang, Q.; Li, T. T.; Hu, Y.; Qian, J. J.; Huang, S. M. Bimetallic AgNi nanoparticles anchored onto MOF-derived nitrogen-doped carbon nanostrips for efficient hydrogen evolution. *Green Energy Environ.* **2023**, *8*, 258–266.
- (29) Guo, B. S.; Zhang, X. M.; Cen, X.; Chen, B.; Wang, X. H.; Song, M.; Ni, S.; Yi, J. H.; Shen, T.; Du, Y. Enhanced mechanical properties of aluminum based composites reinforced by chemically oxidized carbon nanotubes. *Carbon* **2018**, *139*, 459–471.
- (30) Guo, Y. Y.; Huang, Q.; Ding, J. Y.; Zhong, L.; Li, T. T.; Pan, J. Q.; Hu, Y.; Qian, J. J.; Huang, S. M. CoMo carbide/nitride from bimetallic MOF precursors for enhanced OER performance. *Int. J. Hydrogen Energy* **2021**, *46*, 22268–22276.
- (31) Li, J.; Zhou, Y. Y.; Xiao, X.; Wang, W.; Wang, N.; Qian, W. Z.; Chu, W. Regulation of Ni-CNT Interaction on Mn-Promoted Nickel Nanocatalysts Supported on Oxygenated CNTs for CO₂ Selective Hydrogenation. *ACS Appl. Mater. Interfaces* **2018**, *10*, 41224–41236.
- (32) Song, S.; Yao, S. K.; Cao, J. H.; Di, L.; Wu, G. J.; Guan, N. J.; Li, L. D. Heterostructured Ni/NiO composite as a robust catalyst for the hydrogenation of levulinic acid to γ -valerolactone. *Appl. Catal. B: Environ.* **2017**, *217*, 115–124.
- (33) Ren, X. R.; Zhai, Y. Y.; Zhou, Q.; Yan, J. Q.; Liu, S. Z. Fabrication of nanoporous Ni and NiO via a dealloying strategy for water oxidation catalysis. *J. Energy Chem.* **2020**, *50*, 125–134.
- (34) Yazdi, A. Z.; Chizari, K.; Jalilov, A. S.; Tour, J.; Sundararaj, U. Helical and Dendritic Unzipping of Carbon Nanotubes: A Route to Nitrogen-Doped Graphene Nanoribbons. *ACS Nano* **2015**, *9*, 5833–5845.
- (35) Wei, G. L.; Dong, J.; Bai, J.; Zhao, Y. S.; Li, Y. Structurally Stable, Antifouling, and Easily Renewable Reduced Graphene Oxide Membrane with a Carbon Nanotube Protective Layer. *Environ. Sci. Technol.* **2019**, *53*, 11896–11903.
- (36) Liu, C.; Cheng, H. M. Controlled Growth of Semiconducting and Metallic Single-Wall Carbon Nanotubes. *J. Am. Chem. Soc.* **2016**, *138*, 6690–6698.
- (37) Shu, Y.; Yan, Y.; Chen, J. Y.; Xu, Q.; Pang, H.; Hu, X. Y. Ni and NiO Nanoparticles Decorated Metal-Organic Framework Nanosheets: Facile Synthesis and High-Performance Nonenzymatic Glucose Detection in Human Serum. *ACS Appl. Mater. Interfaces* **2017**, *9*, 22342–22349.
- (38) Qiao, Y. X.; Liu, Q.; Lu, S. Y.; Chen, G.; Gao, S. Y.; Lu, W. B.; Sun, X. P. High-performance non-enzymatic glucose detection: using a conductive Ni-MOF as an electrocatalyst. *J. Mater. Chem. B* **2020**, *8*, 5411–5415.
- (39) Ma, Z. Z.; Ma, Y.; Liu, B.; Xu, L.; Jiao, H. A high-performance Co-MOF non-enzymatic electrochemical sensor for glucose detection. *New J. Chem.* **2021**, *45*, 21350–21358.
- (40) Chai, L. L.; Wang, X.; Hu, Y.; Li, X. F.; Huang, S. M.; Pan, J. Q.; Qian, J. J.; Sun, X. L. In-MOF-Derived Hierarchically Hollow Carbon Nanostraws for Advanced Zinc-Iodine Batteries. *Adv. Sci.* **2022**, *9*, 2105063.

(41) Nie, H. G.; Yao, Z.; Zhou, X. M.; Yang, Z.; Huang, S. M. Nonenzymatic electrochemical detection of glucose using well-distributed nickel nanoparticles on straight multi-walled carbon nanotubes. *Biosens. Bioelectron.* **2011**, *30*, 28–34.

Recommended by ACS

Bimetals Ni–Mo–S-Modified Hollow Cubic Cu_{2-x}S for Visible-Light Photocatalytic H₂ Evolution

Ning Li, Lei Ge, *et al.*

APRIL 19, 2023
INORGANIC CHEMISTRY

READ 

Boosting the Activity of the Oxygen Evolution Reaction through an Electrospun Nickel Manganese-Based Bimetallic Zeolite Imidazolate Framework Fibrous System in Alkali...

Sam Sankar Selvasundarasekar, Subrata Kundu, *et al.*

APRIL 10, 2023
INORGANIC CHEMISTRY

READ 

High-Density NiCu Bimetallic Phosphide Nanosheet Clusters Constructed by Cu-Induced Effect Boost Total Urea Hydrolysis for Hydrogen Production

Xiao Xu, Rongfang Wang, *et al.*

MARCH 09, 2023
INORGANIC CHEMISTRY

READ 

Divalent Oxidation State Ni as an Active Intermediate in Prussian Blue Analogues for Electrocatalytic Urea Oxidation

Xiaofang Liu, Jianmei Lu, *et al.*

FEBRUARY 15, 2023
INORGANIC CHEMISTRY

READ 

Get More Suggestions >